CD8+ lymphocytes modulate Zika virus dynamics and tissue dissemination and orchestrate antiviral immunity

Blake Schouest[1,2], Marissa Fahlberg[3], Elizabeth A. Scheef[2], Matthew J. Ward[4], Kyra Headrick[4], Dawn M. Szeltner[2], Robert V. Blair[5], Margaret H. Gilbert[6], Lara A. Doyle-Meyers[6], Victoria W. Danner[6], Myrna C. Bonaldo[7], Dawn M. Wesson[4], Antonito T. Panganiban[2,8], Nicholas J. Maness[2,8]*

[1]Biomedical Sciences Training Program, Tulane University School of Medicine, New Orleans LA 70112

[2]Division of Microbiology, Tulane National Primate Research Center, Covington LA 70433

[3]Division of Immunology, Tulane National Primate Research Center, Covington LA 70433

[4]School of Public Health and Tropical Medicine, Tulane University, New Orleans LA 70112

[5]Division of Comparative Pathology, Tulane National Primate Research Center, Covington LA 70433

[6]Division of Veterinary Medicine, Tulane National Primate Research Center, Covington LA 70433

[7]Laboratório de Biologia Molecular de Flavivírus, Instituto Oswaldo Cruz, Fiocruz, Rio de Janeiro, RJ, Brazil

[8]Department of Microbiology and Immunology, Tulane University School of Medicine, New Orleans LA 70112

*Corresponding author, Nicholas J Maness, nmaness@tulane.edu

Abstract

CD8+ lymphocytes are critically important in the control of viral infections, but their roles in acute Zika virus (ZIKV) infection remain incompletely explored in a model sufficiently similar to humans immunologically. Here, we use CD8+ lymphocyte depletion to dissect acute immune responses in adult male rhesus and cynomolgus macaques infected with ZIKV. CD8 depletion delayed serum viremia and dysregulated patterns of innate immune cell homing and monocyte-driven transcriptional responses in the blood. CD8-depleted macaques also showed evidence of compensatory adaptive immune responses, with elevated Th1 activity and persistence of neutralizing antibodies beyond the clearance of serum viremia. The absence of CD8+ lymphocytes increased viral burdens in lymphatic tissues, semen, and cerebrospinal fluid, and neural lesions were also evident in both CD8-depleted rhesus macaques. Together, these data support a role for CD8+ lymphocytes in the control of ZIKV dissemination and in maintaining immune regulation during acute infection of nonhuman primates.

Introduction

ZIKV has been a known pathogen for over half a century [1], but severe manifestations of the disease were not directly associated with the virus for most of its history. Although recent outbreaks of ZIKV in the Western hemisphere are notorious for neurological complications including congenital Zika syndrome (CZS) and Guillain-Barré syndrome (GBS), most cases remain asymptomatic, and when symptoms arise, they are usually mild and self-limiting [2]. Differential immune responses to ZIKV infection may dictate the severity of accompanying diseases and underlie clinical outcomes.

As the immunological correlates of protection against ZIKV are beginning to be explored, the CD8 T cell response is emerging as an important mediator of viral control, as is true with other flaviviruses [3]. Studies in mice have identified CD8 T cell responses to ZIKV infection, but the induction of ZIKV-associated pathology in these models requires deficiency in type-I interferon (IFN) signaling [4,5], which is not representative of natural ZIKV infection in humans. This is perhaps an unavoidable caveat, as ZIKV is incapable of antagonizing type-I IFN signaling in mice as it does in humans due to a lack of recognition of murine STAT2 by ZIKV NS5 [6]. Disrupting IFN-I signaling, either genetically or through antibody blockade is, therefore, necessary to recapitulate ZIKV neurotropism in mouse models. Importantly, these studies have described dual protective and deleterious effects of CD8 T cell responses in ZIKV infected mice. While CD8+ lymphocyte infiltration appears to reduce viral burdens in the brain, spinal cord and lymphatic tissue [4,5], under certain circumstances, CD8+ influx may also promote immunopathology, evidenced by neural damage and paralysis [7]. However, these findings have yet to be replicated in a model sufficiently similar to humans genetically and immunologically. Given the recent development of rhesus [8-12] and cynomolgus [12,13] macaque models of ZIKV infection, we sought to explore the role of CD8+ lymphocytes in acute ZIKV infection by way of CD8+ lymphocyte depletion. CD8+ depletion is a well-established immune manipulation in nonhuman primates [14] and is thus a plausible approach to gauge how the absence of CD8+ cells impacts acute viremia and potentially modulates adaptive responses.

In the present study, we infected four adult male rhesus macaques and five adult male cynomolgus macaques with a minimally passaged Brazilian ZIKV strain. Prior to infection, two animals of each species were depleted of CD8+ lymphocytes, including CD8 T cells and NK cells. The absence of CD8+ lymphocytes resulted in striking virus-response patterns that were not evident in nondepleted macaques, including delayed serum viremia, enhanced viral dissemination to peripheral tissues, and global repression of antiviral gene transcription. CD8-depleted rhesus macaques also manifested brainstem lesions that were characterized by increased inflammation. Finally, the absence of CD8+ lymphocytes appeared to alter patterns of monocyte expansion and activation and induce compensatory adaptive responses, characterized by enhanced Th1 phenotypes and prolonged neutralizing antibody production.

Results

Delayed serum viremia and altered leukocyte kinetics

CD8+ lymphocyte depletion commenced 14 days prior to ZIKV infection (Fig. 1a), and CD8 T cells were undetectable in all depleted animals well before infection (Fig. 1b). To achieve CD8 depletion, we used the MT807R1 antibody [14] to target CD8α, effectively depleting CD8 T cells (Fig. 1b & Supplementary Fig. 1a), CD8+/CD4+ double-positive T cells (Supplementary Fig. 1b), and NK cells (Fig. 1c) but not CD4 T cells (Supplementary Fig. 1c) from the blood of all treated animals. As MT807R1 targets NK cells in addition to CD8+ lymphocytes, any deficiency in host response following treatment with anti-CD8α could indicate that either or both types of cells are important for acute control of ZIKV. Flow cytometric analysis of NK cell frequency in nondepleted animals revealed expansion early in infection (Fig. 1c). Intriguingly, the CD8-depleted macaque R64357 recovered NK cells and CD8 T cells at later timepoints, between 15 and 21 days post-infection (dpi) (Fig. 1c & Supplementary Fig. 1a).

Following subcutaneous inoculation with ZIKV, nondepleted animals and a single CD8-depleted cynomolgus macaque experienced rapid serum viremia of 3-4.5 logs at 1 dpi (Fig. 1d), consistent with previous reports of ZIKV in both rhesus and cynomolgus macaques [8,13,15]. Strikingly, serum viremia in 3

of 4 CD8-depleted macaques was delayed until 2 dpi, when viral RNA was higher than in nondepleted animals (Fig. 1d). Viremia was also delayed until 3 dpi in C46456 (Fig. 1d), a nondepleted cynomolgus macaque that had been previously splenectomized. Perhaps importantly, the spleen is a major site of replication and spread of the related mosquito-borne flaviviruses dengue virus (DENV) [16] and West Nile virus (WNV) [17] and is also an immense reservoir of monocytes [18], which are permissive to ZIKV replication in humans [19] and macaques [20]. The lack of a spleen in C46456 might have precluded ZIKV replication in this important target organ, thereby delaying viral kinetics.

By 7 dpi, serum viremia persisted in the CD8-depleted cynomolgus macaques in addition to the mock-depleted control, while viremia was undetected in both nondepleted animals of the cohort (Fig. 1d). For the remainder of the study, viral kinetics were similar among cohorts and treatment conditions, peaking at 3 dpi and dropping to undetectable levels by 10 dpi and beyond (Fig. 1d). This was again in exception to C46456, which showed a small viral rebound at 10 dpi. A previous cohort of female macaques infected with the identical strain of ZIKV demonstrated similar patterns of serum viremia to those observed in nondepleted animals (Supplementary Fig. 2a).

The previous female cohort also showed consistent patterns of innate immune cell recruitment in the blood one day following ZIKV infection, summarized by the biomarker neutrophil-to-lymphocyte ratio (NLR) [21]. Patterns of leukocyte mobilization included a spike in neutrophil frequency (Supplementary Fig. 2c) and a simultaneous drop in lymphocyte frequency (Supplementary Fig. 2d), resulting in an elevated NLR at 1 dpi (Supplementary Fig. 2e). These findings were generally recapitulated in nondepleted animals but not in CD8-depleted animals (Figs. 1e-f and Supplementary Figs. 2c-e), potentially linking NLR and acute serum viremia. This association is strengthened by prototypical patterns of leukocyte homing in C78777 (Fig. 1e), the only CD8-depleted macaque with serum viremia at 1 dpi (Fig. 1d).

Differential monocyte-driven transcriptional profiles

To characterize immune responses that might be differentiating patterns of viremia and leukocyte mobilization, we used the NanoString platform to quantify the expression of macaque immune-related genes in whole blood. CD8-depleted and nondepleted animals showed highly divergent profiles in genes related to IFNα signaling (Fig. 2a) and leukocyte homing (Supplementary Fig. 3a), resulting in the robust induction of disease-related pathways in nondepleted macaques that failed to activate in animals lacking CD8+ lymphocytes (Supplementary Fig. 3b). To confirm the transcriptional quiescence evident in CD8-depleted macaques, we used a quantitative real-time PCR (qRT-PCR) array of 84 antiviral genes in the rhesus macaque genome. Consistent with the NanoString results, nondepleted rhesus and cynomolgus macaques showed strong induction of several RIG-I like receptors (RLRs) and type-I IFN stimulated genes (ISGs) at 3 dpi, synchronous with peak serum viremia (Fig. 2b). The most highly induced genes include the pattern recognition receptors *TLR3*, *DDX58* (also known as *RIG-I*), and *IFIH1* (also known as *MDA5*), as well as the ISGs *ISG15*, *MX1*, and *OAS2*. Principal component analysis (PCA) of antiviral signaling further discriminated the transcriptional phenotypes in CD8-depleted and nondepleted animals (Fig. 2c). The induction of antiviral genes in nondepleted rhesus macaques was highest at 3 dpi and was generally followed by a return to near-baseline expression by 15 dpi (Supplementary Fig. 3c). In contrast to nondepleted animals, CD8-depleted macaques showed a virtual absence of transcriptional responses in whole blood at all timepoints tested (Figs. 2a-b and Supplementary Fig. 3d).

Although we suspected monocytes to be driving antiviral gene expression owing to their susceptibility to ZIKV infection [19,20], an important caveat of probing whole blood is that the identity of the transcriptionally responsive cell types is unknown. To resolve cell populations contributing to antiviral signaling in blood, we sorted CD14+ monocytes from peripheral blood mononuclear cells (PBMCs) at 3 dpi and profiled their expression of immune genes. Probe hybridization revealed selective antiviral gene expression in the monocytes of a nondepleted macaque and showed that even purified and sorted PBMCs from a CD8-depleted animal fail to establish transcriptional responses at peak serum viremia (Fig. 2d).

These findings were verified by qRT-PCR (Fig. 2e). Nonetheless, it remained possible that the lack of a transcriptional response in CD8-depleted macaques could have been attributed in part to an absence of otherwise responding NK cells. Sorting transcriptionally responsive PBMCs from a nondepleted rhesus macaque into CD8+ and CD8- fractions, we found similar levels of gene induction in both populations, although expression was marginally higher in the CD8- subset, and transcription of *DDX58* was almost exclusive to CD8- cells (Fig. 2f). Gene induction in CD8+ cells indicates that NK cells may indeed contribute to antiviral signaling, but similar transcriptional activation in the CD8- fraction affirms that the absence of transcriptional activation in CD8-depleted animals was not simply the product of a lack of NK cells.

To further explore innate immune activation in ZIKV-infected myeloid cells, we cultured monocyte-derived macrophages (MDMs) from ZIKV-naïve rhesus macaques *in vitro*, infected the macrophages with ZIKV, and profiled antiviral gene expression using qRT-PCR. We found highly overlapping transcriptional patterns to those observed in the blood of nondepleted macaques at 3 dpi (Fig. 2g), suggesting that ZIKV-permissive myeloid cells may be driving antiviral gene induction *in vivo*.

Altered monocyte activation and frequency

Divergent transcriptional patterns in CD8-depleted and nondepleted macaques could be induced by differentially responding monocytes, given that monocytes are known targets of ZIKV infection [20,22] and contribute to antiviral signaling during ZIKV infection [22]. To interrogate the immunophenotypic effects of CD8 depletion, we developed a multicolor flow cytometry panel to track innate and adaptive immune cells over time. The resulting data were highly dimensional, comprising a variety of surface markers and sampling animals at multiple timepoints and with respect to different treatment groups. To survey general immune responses over time, we used an adaptation of t-distributed stochastic neighbor embedding (tSNE), viSNE [23].

In both rhesus and cynomolgus macaques, CD8 depletion dysregulated the kinetics of monocyte activation as measured by CD169 (siglec-1) expression. Nondepleted rhesus and cynomolgus macaques showed early activation of monocytes, peaking at 3 dpi and returning sharply to baseline by 14-15 dpi (Figs. 3a-c). Upregulation of CD169 in nondepleted animals was affirmed at the RNA level (Fig. 2a). Although patterns of CD169 induction were consistent in all monocyte subsets (Supplementary Figs. 4a-c), viSNE analysis indicated that CD169 was most highly expressed on intermediate and nonclassical monocytes in both cohorts (Figs. 3a-b). Contrasting nondepleted animals, CD8-depleted rhesus and cynomolgus macaques showed less well-defined monocyte activation at 3 dpi, which was accompanied in rhesus macaques by prolonged monocyte activation beyond 15 dpi (Figs. 3a-c & Supplementary Figs. 4a-d). These findings were consistent transcriptionally, as whole blood from CD8-depleted animals had muted expression of genes related to myeloid cell activation (Fig. 3d). Monocyte subsets showed additional nuances in phenotype that appeared dependent on CD8 depletion: In rhesus macaques, CD95 (Fas) was increased on classical monocytes in CD8-depleted animals (Supplementary Fig. 4e) and on nonclassical monocytes in nondepleted animals (Supplementary Fig. 4f).

CD8 depletion also differentially modulated the abundance of monocyte subsets in blood. One day following ZIKV infection, classical monocytes expanded immediately in nondepleted animals of both cohorts (Fig. 3e). During acute infection (3-7 dpi), the frequency of nonclassical monocytes increased preferentially in CD8-depleted rhesus macaques and in nondepleted cynomolgus macaques (Fig. 3f). Nondepleted rhesus macaques showed an expansion of intermediate monocyte frequency at 3-7 dpi (Fig. 3g), although a CD8-dependent effect on intermediate monocyte frequency was not evident in cynomolgus monkeys.

Compensatory adaptive immune responses

Adaptive immune responses to ZIKV were also differentially modulated by CD8 depletion, with apparent compensatory responses in CD8-depleted macaques of both cohorts. Nondepleted rhesus and cynomolgus macaques consistently induced CD8 T cell responses 7-10 dpi, which were characterized by proliferation

(Ki67) and activation (CD69) of effector memory (EM), central memory (CM), and naïve CD8 T cell subsets (Figs. 4a-c & Supplementary Figs 5a-e). These responses were antigen-specific and functional, given that CD8 T cells stimulated with ZIKV peptides produced IFNγ and contained perforin by intracellular cytokine staining (ICS) (Fig. 4e). Intriguingly, the CD8-depleted rhesus macaque R64357 also showed evidence of a CD8 T cell response at 21 dpi (Figs. 4c & 4e), concomitant with the recovery of CD8+ lymphocytes in this animal (Supplementary Fig. 1a).

The absence of CD8 T cells in depleted rhesus and cynomolgus macaques appeared to promote the reciprocal activation and expansion of CD4 T cell subsets (Figs. 4a-b, 4d and Supplementary Figs. 5f-j), mirroring the kinetics of CD8 T cell activation in nondepleted animals. CD4 T cell responses were Th1 in functionality, characterized by co-positivity for IL-2 and IFNγ, and were also antigen-specific for E and NS1 peptides in both CD8-depleted rhesus macaques (Fig. 4f).

To gauge humoral responses to ZIKV, we conducted a plaque reduction neutralization test (PRNT) using rhesus macaque sera to quantify neutralizing antibody titers. All animals except R20865 showed evidence of neutralizing antibodies at 7 dpi, the earliest post-infection timepoint tested (Fig. 4g). While highly neutralizing titers were present in all animals at 15 dpi, antibody concentrations declined in nondepleted animals, but not in CD8-depleted animals, beyond this timepoint. Strikingly, depleted rhesus macaques retained highly neutralizing antibody titers until necropsy, a finding consistent with elevated B cell proliferation (Fig. 4h) and activation (Fig. 4i) in these animals.

Enhanced tissue dissemination and neuropathology

Given the persistence of high neutralizing antibody titers in CD8-depleted rhesus macaques, we suspected that virus might be lingering in the peripheral tissues of these animals. The duration of infection before necropsy differed among the rhesus (30 dpi) and cynomolgus (14 dpi) macaque cohorts to identify patterns of viral dissemination and clearance over time. Informed by previous reports of ZIKV tropism in

macaques [10,15,24], we searched for viral RNA in lymphoid, neural, gastrointestinal (GI), and reproductive tissues, as well as in semen and cerebrospinal fluid (CSF) to evaluate viral distribution in these sites.

Relative to nondepleted animals, CD8-depleted cynomolgus macaques had markedly higher levels of ZIKV RNA in the inguinal, mesenteric, and colonic lymph nodes, as well as in the spleen and jejunum (Figs. 5a and 5c). All cynomolgus monkeys except C91638 harbored virus in the rectum without an obvious difference among treatment groups. Notably, the trend of higher viral burdens in the lymphatic tissues of CD8-depleted animals was consistent in rhesus macaques (Fig. 5f). CD8 depletion also appeared to promote ZIKV dissemination in the semen, with both CD8-depleted cynomolgus macaques presenting semen viral loads and no viral RNA detected in nondepleted animals of the same cohort (Fig. 5d). Intriguingly, the nondepleted macaque C84545 showed the highest level of viral RNA in the prostate and was the only animal to present virus in the testes (Fig. 5c), yet no ZIKV was detected in the semen of this animal (Fig. 5d). These findings too were consistent in rhesus macaques, with virus detected in the semen (Fig. 5g) and seminal vesicle (Fig. 5f) of a CD8-depleted animal and only a miniscule quantity of viral RNA detected in the semen of a nondepleted animal (Fig. 5g).

ZIKV RNA was detected in the brainstem and subcortical white matter of C84545 (Fig. 5b), and this animal also presented a high magnitude viral load in the CSF early in infection, which persisted until necropsy (Fig. 5e). Exclusive of C84545, CD8-depleted cynomolgus and rhesus macaques manifested CSF viral loads at least an order of magnitude greater than nondepleted animals (Figs. 5e and 5h). Although ZIKV was not detected in the CNS of any rhesus macaque, R25671 and R64357 manifested neural lesions at necropsy that were not present in nondepleted animals. Most strikingly, the brainstem of R25671 showed an area of severe multifocal to coalescing encephalomalacia which showed evidence of Wallerian degeneration, characterized by vacuolation, swollen axons, and infiltration by lymphocytes and phagocytic gitter cells (Fig. 5i). Gitter cells are occasionally found within dilated myelin sheaths. Scant brown granular pigment (presumed hemosiderin) and a proliferative cerebral vessel adjacent to the malacia may indicate that the malacia is the result of a vascular event (thromboembolism, infarct,

ischemia, etc.). Additionally, lymphocytic infiltrate was present in the meninges surrounding the lumbar spinal cord (Fig. 5i). No gross abnormalities were noted in R64357, although the sciatic nerve exhibited mild lymphocytic perivasculitis. The sciatic nerve is a known site of ZIKV replication in mice depleted of CD8 cells [4]. Further, the brainstem contained a localized area of gliosis, an indicator of CNS damage[25], and dilated myelin sheaths (Fig. 5j). A cause for these neural inflammatory lesions was not apparent by histology.

Discussion

Owing to the importance of CD8+ T cells in the control of ZIKV in mice [4,5], our aim was to explore whether these findings are consistent in nonhuman primates. The absence of CD8+ lymphocytes prompted immediately observable host responses that diverged from previously consistent patterns of viremia and immunity. The delay of serum viremia in CD8-depleted macaques stood in patent contrast to patterns of acute ZIKV infection observed by our own group (Supplementary Fig. 2a) and others [8]. Although a mechanism underlying the delayed serum viremia remains obscure, it is possible that a lack of NK cell stimulation in CD8-depleted animals may be misfiring viral replication in what would otherwise be readily permissive monocytes. Indeed, monocytes engage in intercellular crosstalk with NK cells [26,27], and IFNγ is shown to support ZIKV replication [28]. NK cell-derived IFNγ may activate ZIKV infected myeloid cells in nondepleted animals, promoting an inflammatory milieu that favors early viral replication. Alternatively, NK cells are shown to be minor reservoirs of ZIKV RNA in infected humans [19] and pigtail macaques [20], so the absence of this potential target cell may contribute to the delayed serum viremia in CD8-depleted animals.

CD8 depletion also impacted the mobilization of leukocyte populations acutely following infection, contrasting patterns reliably observed by our own group (Figs S2c-e) and others [15]. Macaques depleted of CD8 T cells and NK cells show little fluctuation in the biomarker of inflammation NLR, indicating altered innate immune responses immediately following infection. In line with these observations, mice

lacking NK cells exhibit altered neutrophil recruitment in a variety of infectious and noninfectious conditions [29]. Neutrophil effector functions are modulated by NK cell-derived cytokines [29], a signaling axis which might have been disrupted by the depletion of NK cells in macaques.

Confirming miscommunication within the innate immune system of CD8-depleted macaques, these animals presented largely muted transcriptional activity in key virus response pathways during acute infection. In nondepleted macaques, antiviral gene expression was driven principally by circulating monocytes, which stood in sharp contrast to the transcriptional void evident in CD8-depleted animals. Intercellular crosstalk between monocytes and NK cells affects transcriptional responses to ZIKV infection [22], so the absence of NK cells in CD8-depleted macaques might have permitted the infection to evade transcriptional induction in monocytes, complementing the delayed viremia in these animals.

Consistent with a model of monocyte-dependent outcomes in acute ZIKV infection, CD8-depleted and nondepleted macaques also differed in the magnitude and phenotype of their monocyte responses during acute infection. Intermediate and nonclassical monocytes showed the greatest degree of activation, agreeing with recent findings that these subsets are primary targets of ZIKV in the blood [19,30,31]. CD8 depletion also impacted the activation of monocytes temporally, further underscoring dysregulated innate responses in depleted animals. CD169 (siglec-1) is a sialic acid-binding lectin previously found to be upregulated in acute ZIKV infection in rhesus macaques [24,32]. CD169 has important roles in virus capture by myeloid cells [33] and in the mounting of CD8 T cell responses in viral infection [34], so the robust induction of CD169 in nondepleted animals might have promoted sufficient CD8 T cell responses. CD8 depletion also affected monocyte frequency, possibly contributing to differential transcriptional responses. The transient increase in classical monocytes of both cohorts may be analogous to the monocytosis that accompanies acute ZIKV replication in human patients [19]. The increase in CD16+ nonclassical monocytes in CD8-depleted rhesus macaques is an outcome also observed in ZIKV infection of human blood [30], and the expansion of intermediate monocytes in nondepleted animals resembles ZIKV

273 infection in Nicaraguan patients [19]. Our data support a CD8+ lymphocyte-dependent effect in these
274 transitions, possibly accounting for divergent transcriptional responses in blood.

275 In addition to modulating innate immune responses, the depletion of CD8+ lymphocytes also promoted
276 compensatory adaptive responses to ZIKV in both cohorts. Nondepleted animals and even the CD8-
277 recovering rhesus macaque R64357 mounted robust CD8 T cell responses, affirming the importance of
278 CD8+ lymphocytes in acute infection. There is precedence for CD8 T cell responses to ZIKV in mice [4,5,35]
279 and humans [36,37], which appears to be consistent in nonhuman primates. Meanwhile, the presence of Th1
280 responses and prolonged humoral responses in CD8-depleted animals possibly compensate for the
281 absence of CD8 surveillance. Such adaptive responses are reported in mice, as Th1 polarization [35], and
282 CD4-driven humoral responses [38] are important for controlling infection. Our data support the importance
283 of these adaptive responses in nonhuman primates, especially when the CD8 arm of adaptive immunity is
284 compromised.

285 The persistence of high neutralizing antibody titers until necropsy in CD8-depleted rhesus macaques also
286 suggested that there might be virus lingering in the peripheral tissues of these animals. Indeed, ZIKV
287 RNA was generally more abundant in the lymphatic tissues, semen and CSF of CD8-depleted rhesus and
288 cynomolgus macaques relative to nondepleted animals, implying the importance of CD8+ lymphocytes in
289 limiting ZIKV dissemination and/or persistence in tissues. Tissue viral loads were also consistently higher
290 in cynomolgus compared to rhesus macaques, possibly reflecting the abbreviated time of infection before
291 necropsy. In rhesus monkeys, it is possible that the absence of viral RNA in neural and reproductive
292 tissues might have been transient due to viral clearance given the 30-day infection period of these
293 animals. Previous reports in rhesus [39] and pigtail [20] monkeys have also shown that ZIKV persists in
294 lymphatic tissues well beyond the clearance of virus from the serum. Although it remains unclear whether
295 the ZIKV present in lymph nodes is replication competent, our data are nonetheless consistent with a
296 model where the absence of CD8+ lymphocytes permits the dispersal of ZIKV.

297 CD8-depleted rhesus macaques also presented gross neural lesions at necropsy not seen in nondepleted
298 animals. The most severe lesion occurred in the brainstem of a depleted animal that never recovered
299 CD8+ lymphocytes, and similar manifestations of encephalomalacia and axon degeneration have been
300 reported in ZIKV infection of human fetal brain tissue [40-42]. Perhaps complementarily, neural lesions in
301 the CD8-recovering rhesus macaque were less severe. Although it is tempting to speculate that the
302 absence of CD8+ lymphocytes in R25671 and R64357 allowed neural dissemination of the virus and
303 thereby promoted neuropathy, our inability to detect ZIKV RNA in brain sections from these animals
304 precludes this conclusion. Because ZIKV was cleared from the CSF of rhesus monkeys within 15 dpi, it is
305 possible that virus could have also cleared from the CNS by necropsy and that these lesions were virus
306 associated even if viral RNA was not detectable late in infection. Supporting this argument, CSF viral
307 loads appear to be associated with ZIKV dissemination in neural tissue, given that C84545 showed the
308 highest and most persistent CSF viremia and was also the only animal with ZIKV RNA identified in the
309 brain. The absence of immune surveillance and IFN signaling in depleted animals might have permitted
310 initial ZIKV infection of neural tissues, but infection could have been transient due to the eventual
311 priming of compensatory adaptive responses. Additionally, ZIKV localizes as discrete foci in macaque
312 tissues [32], complicating the detection of sparse viral lesions within organs. It is worth noting that CNS
313 localization of ZIKV has been observed as early as 5 dpi in acutely infected macaques [15], and a separate
314 study in rhesus monkeys failed to identify ZIKV RNA in the CNS at 14 dpi, despite diffuse patterns of
315 viral dissemination [10]. These findings, together with our own, establish precedence for early CNS
316 dissemination of ZIKV in nonhuman primates, which may be cleared later in infection.

317 In summary, the present study illustrates a pliable dynamic between ZIKV and its hosts. CD8 depletion
318 appears to alter patterns of innate immune activation and regulation, possibly disrupting patterns of
319 antiviral signaling. CD8 T cells may provide default adaptive immune responses to ZIKV, and their
320 absence may induce compensatory CD4 and humoral responses. Finally, CD8+ lymphocytes appear to

constitute frontline defenses to ZIKV, potentially limiting viral dissemination to lymphoid tissues, reproductive organs, and the CNS.

Methods

Animal experiments

The four adult male Indian origin rhesus macaques (*Macaca mulatta*) and five adult male cynomolgus macaques (*Macaca fascicularis*) utilized in this study were housed at the Tulane National Primate Research Center (TNPRC). The TNPRC is fully accredited by AAALAC International (Association for the Assessment and Accreditation of Laboratory Animal Care), Animal Welfare Assurance No. A3180-01. Animals were cared for in accordance with the NRC Guide for the Care and Use of Laboratory Animals and the Animal Welfare Act Animal experiments were approved by the Institutional Animal Care and Use Committee of Tulane University (protocol P0367).

Two rhesus macaques (R25671 and R64357) and two cynomolgus macaques (C78777 and C18942) were depleted of CD8+ lymphocytes by administration of the anti-CD8α antibody MT807R1 (NHP Reagent Resource; https://www.nhpreagents.org) [14]. The initial subcutaneous administration of 10 mg/kg at 14 days pre-infection was followed by three intravenous administrations of 5 mg/kg at 11, 7, and 5 days pre-infection, as per the distributor's protocol. C84545 was treated with the irrelevant control antibody anti-desmipramine (NHP Reagent Resource; https://www.nhpreagents.org) at the same dosages and time intervals pre-infection. All animals were subcutaneously infected with 10^4 PFU of a Brazilian ZIKV isolate [43] at 0 dpi (Fig. 1a). For data comparison, we included viral loads and complete blood count (CBC) data from a previous cohort of 4 non-pregnant female rhesus macaques (R32835, R24547, R25508, R22624) that were similarly infected with the same dose of the same Brazilian ZIKV isolate that was used in this study (Supplementary Figs. 2a-e).

Whole blood, CSF, and semen were obtained from animals at the indicated timepoints (Fig. 1a). PBMCs were isolated from the blood of rhesus macaques using SepMate tubes (Stemcell Technologies) according to the manufacturer's protocol or from the blood of cynomolgus macaques using Lymphoprep (Stemcell Technologies) for standard density gradient centrifugation. At necropsy, the indicated tissues were collected and snap-frozen.

Virus quantification

Viral RNA was extracted from serum and CSF using the High Pure Viral RNA Kit (Roche). Semen, as well as the indicated lymphoid, reproductive, GI, and neural tissues were homogenized in Qiazol (Qiagen) using either disposable tissue grinders (Fisherbrand) or a TissueRuptor (Qiagen), and RNA was isolated using the RNeasy Lipid Tissue Mini Kit (Qiagen). Viral RNA from body fluids and tissues was quantified using qRT-PCR as described previously [44].

Antiviral gene expression assays

2.5 ml whole blood was drawn from each animal at 0, 1, 3, and 15 dpi into PAXgene blood RNA tubes (PreAnalytiX) and equilibrated to -80˚C as per the manufacturer's protocol. RNA was extracted from blood samples using the PAXgene blood RNA kit (PreAnalytiX), and cDNA was synthesized using the RT2 First Strand Kit (Qiagen). Transcriptional profiles of immune signaling were generated using the nCounter NHP Immunology Panel of 770 macaque immune response genes (NanoString Technologies). In whole blood, transcriptional responses were assessed at 3 dpi relative to expression levels pre-infection using nSolver software v4.0 (NanoString Technologies). Fold change data were imported into Ingenuity Pathway Analysis (IPA) (Qiagen) to discern relevant signaling pathways and disease functions. Antiviral transcriptional responses were confirmed by way of qRT-PCR using a rhesus macaque RT2 Profiler PCR Array (Qiagen). Responses within each species and treatment group were analyzed together to identify expression levels at the indicated timepoints relative to pre-infection. Heatmaps of gene expression and

366 disease-related pathways were generated using Morpheus (https://software.broadinstitute.org/Morpheus).
367 PCA of antiviral gene expression was performed using ClustVis [45].

368 To identify cell populations contributing to antiviral signaling in blood, the CD14 and CD8 MicroBead
369 kits (Miltenyi Biotec) were used to sort CD14+ monocytes and CD8+ lymphocytes from the PBMCs of
370 the indicated animals at peak transcriptional activity (3 dpi). RNA was isolated from cell fractions using
371 the RNeasy Mini Kit (Qiagen), and cDNA was synthesized using the RT2 First Strand Kit (Qiagen).
372 Transcriptional profiling was performed using the nCounter NHP Immunology Panel (NanoString) and
373 verified by RT2 qPCR Primer Assays (Qiagen) for ISG15, OAS2, and DDX58.

374 To characterize antiviral signaling in myeloid cells, PBMCs were isolated from the whole blood of 4
375 ZIKV-naïve colony rhesus macaques as described above, and the CD14 MicroBead kit (Miltenyi Biotec)
376 was used to isolate monocytes. Monocytes were cultured at 1×10^6 cells/ml in RPMI-1640 medium
377 supplemented with 1% human AB serum (Sigma), 20 ng/ml M-CSF (Peprotech), 1% L-glutamine, and
378 1% penicillin/streptomycin. After 7 days of culture, monocytes were sufficiently differentiated into
379 macrophages and were either infected with the same Brazilian ZIKV isolate described above or left
380 uninfected. At 24 hpi, RNA was extracted using the RNeasy Mini Kit (Qiagen), cDNA was synthesized
381 using the RT2 First Strand Kit (Qiagen), and transcriptional signaling was assessed using the rhesus
382 macaque antiviral response RT2 Profiler PCR Array (Qiagen). Antiviral gene expression in ZIKV-
383 infected MDMs was calculated relative to uninfected controls.

384 Flow cytometry and gating strategy

385 For absolute lymphocyte counts, whole blood was stained within 2 hours of blood draw for the surface
386 markers CD45 (PerCP; DO58-1283; BD Biosciences), CD3 (FITC; SP34; BD Biosciences), CD4 (APC;
387 L200; BD Biosciences), and CD8 (V500; SK1; BD Biosciences). Flow cytometry was performed on a BD
388 FACSVerse instrument, and absolute counts were calculated using FACS Suite software.

For immunophenotyping, PBMCs from the indicated timepoints were thawed, washed, and stained using Live/Dead Fixable Aqua Dead Cell Stain Kit (Invitrogen). PBMCs were then stained for the surface markers CD16 (AL488; 3G8; BioLegend), CD169 (PE; 7-239; BioLegend), CD28 (PECF594; CD28.2; BD Biosciences), CD95 (PCP-Cy5.5; DX2; BioLegend), CD3 (PE-Cy7; SP34-2; BD Biosciences), CD8 (PacBlue; SK1; BioLegend), CD14 (BV605; M5E2; BD Biosciences), HLA-DR (BV650; L243; BioLegend), NKG2A (APC; Z199; Beckman Coulter), and CD4 (APC-H7; L200; BD Biosciences). Cells were subsequently fixed in FluoroFix buffer (BioLegend), permeabilized using Perm/Wash buffer (BioLegend), and stained intracellularly for CD69 (BV711; FN50; BD Biosciences) and Ki67 (AL700; B56; BD Biosciences). Flow cytometry was performed on a BD LSRII instrument and data were analyzed using FlowJo (vX.10.4.2) and viSNE (Cytobank) softwares. For viSNE analysis, live singlet monocytes (CD14+ and/or CD16+) or live singlet CD3+ T cells were gated prior to downsampling at a minimum of 500 cells per animal in FlowJo v. 10.5.3. Downsampled files for each animal were then concatenated by group (i.e., species, dpi, and treatment condition). When the number of animals differed per group, concatenated files were further downsampled to achieve an equal number of cells per group. viSNE was conducted using Cytobank with the following settings: Perplexity = 30, Iterations = 1000, Theta = 0.5, Seed = random, Compensation = internal file. For the monocyte viSNE, the following parameters were utilized in the run: Ki67, CD14, HLA-DR, CD69, CD95, CD14, and CD169. For the CD3+ T cells viSNE, the following parameters were utilized in the run: Ki67, CD4, HLA-DR, CD69, CD95, CD28, CD3, CD8.

For general immunophenotyping analysis, cytometry data were first gated for lymphocytes, singlets, and live cells. NK cells were considered as CD8+/CD16+. CD4 T cells (CD3+/CD4+) and CD8 T cells (CD3+/CD8+) were gated into naïve (CD28+/CD95-), central memory (CD28+/CD95+), and effector memory (CD28-/CD95+) subsets. CD3- cells were divided into B cells (DR+/CD14-/CD16-) and monocytes (classical, CD14++/CD16-; intermediate, CD14+/CD16+; nonclassical, $CD14^{low}$/CD16+). Cell

subsets were analyzed with respect to frequency, proliferation (Ki67+) and activation (CD69+ or CD169+).

Intracellular cytokine staining

PBMCs from the indicated timepoints were thawed and rested overnight prior to stimulation with peptide pools comprising ZIKV C, M, E, and NS1 (BEI Resources). On peptide stimulation, cells were also treated with brefeldin A (BioLegend), GolgiStop (BD Biosciences), anti-CD28 (NHP Reagent Reference Program, www.nhpreagents.org/), anti-CD49d (9F10; BioLegend), and anti-CD107a (AL700; H4A3; BD Biosciences). 24 hours post-stimulation, cells were stained for the surface markers CD3 (PE-Cy7; SP34-2; BD Biosciences), CD8 (PacBlue; SK1; BioLegend), and CD4 (APC-H7; L200; BD Biosciences). Cells were also fixed and permeabilized as described above and stained intracellularly for perforin (FITC; Pf-344; Mabtech), granzyme B (PE; GB12; Invitrogen), CD69 (PE-CF594; FN50; BD Biosciences), IL-2 (PCP-Cy5.5; MQ1-17H12; BD Biosciences), and IFNγ (AL647; 4S.B3; BioLegend). Flow cytometry was performed on a BD LSRII instrument and data were analyzed using FlowJo software (vX.10.4.2).

Plaque reduction neutralization tests

ZIKV PRNTs were conducted according to previously published protocols [46,47]. Briefly, ZIKV MEX-I-44 isolated in Tapachula, Mexico in 2016 was obtained from The University of Texas Medical Branch, Galveston, TX and cultured to passage 8 in Vero cells. Serum specimens were incubated for one hour at serial dilutions of 1:10, 1:20…1:320 with a previously frozen virus stock of known plaque forming unit (PFU). Samples were then inoculated in duplicate onto a mono-layer of Vero cells grown on 6-well plates and allowed to incubate for an additional hour. Infectious material was then removed and replaced with a 1:1 mixture of Vero media and Avicel® before being incubated for 4 days. To read plaques, the Avicel® layer was fixed with 10% neutral buffered formalin. Finally, the formalin-Avicel® layer was removed and the monolayer was stained with crystal violet, washed with tap water and allowed to dry before plaques were counted manually.

Percent reduction in observed plaques and a PRNT90 cutoff were used for interpretation. A PRNT90 titer is the dilution of a sample at which a 90% reduction in possible plaques is observed. The maximum number of potential plaques was obtained for each run using a corresponding back-titration and a linear model was fit to the observed number of plaques for each dilution. A PRNT90 titer was derived for each sample using the linear model and the equation for a straight line in the statistical program R [48]. For samples that were positive but above the resolution of the PRNT assay the value of the greatest number of possible plaques for that run, as determined by the back titration, was assigned for each dilution for use with the linear model.

Histology

Tissues samples collected at necropsy were fixed in Z-Fix (Anatech), embedded in paraffin and 5 μ m thick sections were cut, adhered to charged glass slides, and either stained routinely with hematoxylin and eosin or Prussian blue.

Statistical analysis

For NLR comparison, the Mann-Whitney test was performed using GraphPad Prism v6.07 (GraphPad Software).

References

1 Dick, G. W., Kitchen, S. F. & Haddow, A. J. Zika virus. I. Isolations and serological specificity. *Trans R Soc Trop Med Hyg* **46**, 509-520 (1952).

2 Plourde, A. R. & Bloch, E. M. A Literature Review of Zika Virus. *Emerg Infect Dis* **22**, 1185-1192, doi:10.3201/eid2207.151990 (2016).

3 Slon Campos, J. L., Mongkolsapaya, J. & Screaton, G. R. The immune response against flaviviruses. *Nat Immunol* **19**, 1189-1198, doi:10.1038/s41590-018-0210-3 (2018).

4 Elong Ngono, A. *et al.* Mapping and Role of the CD8(+) T Cell Response During Primary Zika Virus Infection in Mice. *Cell Host Microbe* **21**, 35-46, doi:10.1016/j.chom.2016.12.010 (2017).

5 Huang, H. *et al.* CD8+ T Cell Immune Response in Immunocompetent Mice during Zika Virus Infection. *J Virol* **91**, doi:10.1128/jvi.00900-17 (2017).

6 Grant, A. *et al.* Zika Virus Targets Human STAT2 to Inhibit Type I Interferon Signaling. *Cell host & microbe* **19**, 882-890, doi:10.1016/j.chom.2016.05.009 (2016).

7 Jurado, K. A. *et al.* Antiviral CD8 T cells induce Zika-virus-associated paralysis in mice. *Nat Microbiol* **3**, 141-147, doi:10.1038/s41564-017-0060-z (2018).

8 Dudley, D. M. *et al.* A rhesus macaque model of Asian-lineage Zika virus infection. *Nat Commun* **7**, 12204, doi:10.1038/ncomms12204 (2016).

9 Dudley, D. M. *et al.* Miscarriage and stillbirth following maternal Zika virus infection in nonhuman primates. *Nature medicine* **24**, 1104-1107, doi:10.1038/s41591-018-0088-5 (2018).

10 Coffey, L. L. *et al.* Zika Virus Tissue and Blood Compartmentalization in Acute Infection of Rhesus Macaques. *PLoS One* **12**, e0171148, doi:10.1371/journal.pone.0171148 (2017).

11 Magnani, D. M. *et al.* Fetal demise and failed antibody therapy during Zika virus infection of pregnant macaques. *Nature communications* **9**, 1624, doi:10.1038/s41467-018-04056-4 (2018).

12 Osuna, C. E. *et al.* Zika viral dynamics and shedding in rhesus and cynomolgus macaques. *Nature medicine* **22**, 1448-1455, doi:10.1038/nm.4206 (2016).

13 Koide, F. *et al.* Development of a Zika Virus Infection Model in Cynomolgus Macaques. *Front Microbiol* **7**, 2028, doi:10.3389/fmicb.2016.02028 (2016).

14 Schmitz, J. E. *et al.* A nonhuman primate model for the selective elimination of CD8+ lymphocytes using a mouse-human chimeric monoclonal antibody. *Am J Pathol* **154**, 1923-1932, doi:10.1016/S0002-9440(10)65450-8 (1999).

15 Osuna, C. E. *et al.* Zika viral dynamics and shedding in rhesus and cynomolgus macaques. *Nat Med* **22**, 1448-1455, doi:10.1038/nm.4206 (2016).

16 Prestwood, T. R. *et al.* Trafficking and replication patterns reveal splenic macrophages as major targets of dengue virus in mice. *J Virol* **86**, 12138-12147, doi:10.1128/JVI.00375-12 (2012).

17 Bryan, M. A. *et al.* Splenic macrophages are required for protective innate immunity against West Nile virus. *PLoS One* **13**, e0191690, doi:10.1371/journal.pone.0191690 (2018).

18 Swirski, F. K. *et al.* Identification of splenic reservoir monocytes and their deployment to inflammatory sites. *Science* **325**, 612-616, doi:10.1126/science.1175202 (2009).

19 Michlmayr, D., Andrade, P., Gonzalez, K., Balmaseda, A. & Harris, E. CD14+CD16+ monocytes are the main target of Zika virus infection in peripheral blood mononuclear cells in a paediatric study in Nicaragua. *Nat Microbiol* **2**, 1462-1470, doi:10.1038/s41564-017-0035-0 (2017).

20 O'Connor, M. A. *et al.* Early cellular innate immune responses drive Zika viral persistence and tissue tropism in pigtail macaques. *Nat Commun* **9**, 3371, doi:10.1038/s41467-018-05826-w (2018).

21 Faria, S. S. *et al.* The neutrophil-to-lymphocyte ratio: a narrative review. *Ecancermedicalscience* **10**, 702, doi:10.3332/ecancer.2016.702 (2016).

22 Lum, F. M. *et al.* Zika Virus Infection Preferentially Counterbalances Human Peripheral Monocyte and/or NK Cell Activity. *mSphere* **3**, doi:10.1128/mSphereDirect.00120-18 (2018).

23 Amir, e.-A. *et al.* viSNE enables visualization of high dimensional single-cell data and reveals phenotypic heterogeneity of leukemia. *Nat Biotechnol* **31**, 545-552, doi:10.1038/nbt.2594 (2013).

24 Hirsch, A. J. *et al.* Zika Virus infection of rhesus macaques leads to viral persistence in multiple tissues. *PLoS pathogens* **13**, e1006219, doi:10.1371/journal.ppat.1006219 (2017).

25 Garman, R. H. Histology of the central nervous system. *Toxicol Pathol* **39**, 22-35, doi:10.1177/0192623310389621 (2011).

26 Michel, T., Hentges, F. & Zimmer, J. Consequences of the crosstalk between monocytes/macrophages and natural killer cells. *Front Immunol* **3**, 403, doi:10.3389/fimmu.2012.00403 (2012).

27 Dalbeth, N. *et al.* CD56bright NK cells are enriched at inflammatory sites and can engage with monocytes in a reciprocal program of activation. *J Immunol* **173**, 6418-6426 (2004).

28 Chaudhary, V. *et al.* Selective Activation of Type II Interferon Signaling by Zika Virus NS5 Protein. *J Virol* **91**, doi:10.1128/JVI.00163-17 (2017).

29 Costantini, C. & Cassatella, M. A. The defensive alliance between neutrophils and NK cells as a novel arm of innate immunity. *J Leukoc Biol* **89**, 221-233, doi:10.1189/jlb.0510250 (2011).

30 Foo, S. S. *et al.* Asian Zika virus strains target CD14+ blood monocytes and induce M2-skewed immunosuppression during pregnancy. *Nat Microbiol* **2**, 1558-1570, doi:10.1038/s41564-017-0016-3 (2017).

31 Jurado, K. A. & Iwasaki, A. Zika virus targets blood monocytes. *Nat Microbiol* **2**, 1460-1461, doi:10.1038/s41564-017-0049-7 (2017).

32 Hirsch, A. J. *et al.* Zika virus infection in pregnant rhesus macaques causes placental dysfunction and immunopathology. *Nat Commun* **9**, 263, doi:10.1038/s41467-017-02499-9 (2018).

33 Sewald, X. *et al.* Retroviruses use CD169-mediated trans-infection of permissive lymphocytes to establish infection. *Science* **350**, 563-567, doi:10.1126/science.aab2749 (2015).

34 van Dinther, D. *et al.* Functional CD169 on Macrophages Mediates Interaction with Dendritic Cells for CD8. *Cell Rep* **22**, 1484-1495, doi:10.1016/j.celrep.2018.01.021 (2018).

35 Pardy, R. D. *et al.* Analysis of the T Cell Response to Zika Virus and Identification of a Novel CD8+ T Cell Epitope in Immunocompetent Mice. *PLoS Pathog* **13**, e1006184, doi:10.1371/journal.ppat.1006184 (2017).

36 Grifoni, A. *et al.* Prior Dengue virus exposure shapes T cell immunity to Zika virus in humans. *J Virol*, doi:10.1128/JVI.01469-17 (2017).

37 Grifoni, A. *et al.* Cutting Edge: Transcriptional Profiling Reveals Multifunctional and Cytotoxic Antiviral Responses of Zika Virus-Specific CD8. *J Immunol* **201**, 3487-3491, doi:10.4049/jimmunol.1801090 (2018).

38 Lucas, C. G. O. *et al.* Critical role of CD4+ T cells and IFNγ signaling in antibody-mediated resistance to Zika virus infection. *Nat Commun* **9**, doi:10.1038/s41467-018-05519-4 (2018).

39 Aid, M. *et al.* Zika Virus Persistence in the Central Nervous System and Lymph Nodes of Rhesus Monkeys. *Cell* **169**, 610-620.e614, doi:10.1016/j.cell.2017.04.008 (2017).

40 Vesnaver, T. V. *et al.* Zika virus associated microcephaly/micrencephaly-fetal brain imaging in comparison with neuropathology. *BJOG* **124**, 521-525, doi:10.1111/1471-0528.14423 (2017).

41 Driggers, R. W. *et al.* Zika Virus Infection with Prolonged Maternal Viremia and Fetal Brain Abnormalities. *N Engl J Med* **374**, 2142-2151, doi:10.1056/NEJMoa1601824 (2016).

42 Petribu, N. C. L. *et al.* Common findings on head computed tomography in neonates with confirmed congenital Zika syndrome. *Radiol Bras* **51**, 366-371, doi:10.1590/0100-3984.2017.0119 (2018).

43 Bonaldo, M. C. *et al.* Isolation of Infective Zika Virus from Urine and Saliva of Patients in Brazil. *PLoS Negl Trop Dis* **10**, e0004816, doi:10.1371/journal.pntd.0004816 (2016).

44 Magnani, D. M. *et al.* Fetal demise and failed antibody therapy during Zika virus infection of pregnant macaques. *Nat Commun* **9**, 1624, doi:10.1038/s41467-018-04056-4 (2018).

45 Metsalu, T. & Vilo, J. ClustVis: a web tool for visualizing clustering of multivariate data using Principal Component Analysis and heatmap. *Nucleic Acids Res* **43**, W566-570, doi:10.1093/nar/gkv468 (2015).

46 Lieberman, M. M. *et al.* Immunogenicity and protective efficacy of a recombinant subunit West Nile virus vaccine in rhesus monkeys. *Clin Vaccine Immunol* **16**, 1332-1337, doi:10.1128/CVI.00119-09 (2009).

47 Ward, M. J. *et al.* Zika Virus and the World Health Organization Criteria for Determining Recent Infection Using Plaque Reduction Neutralization Testing. *Am J Trop Med Hyg* **99**, 780-782, doi:10.4269/ajtmh.18-0237 (2018).

48 R: A language and environment for statistical computing (R Foundation for Statistical Computing, Vienna, Austria, 2018).

Acknowledgements

This work was supported by a pilot award to N.J.M. from the Tulane National Primate Research Center base grant (NIH P51OD011104). The funders had no role in study design and interpretation.

Author contributions

B.S., A.T.P., and N.J.M. planned the studies. B.S., M.F., E.A.S., M.J.W., K.H., D.M.S., R.V.B., M.H.G., L.A.D.M., and V.W.D. conducted the experiments. D.M.W. and M.C.B. provided reagents. B.S., M.F., M.J.W., R.V.B, A.T.P., and N.J.M interpreted the studies. B.S. and N.J.M. wrote the first draft. A.T.P. and N.J.M. obtained funding. All authors reviewed, edited, and approved the paper.

Competing interests

The authors declare no competing interests.

Materials & Correspondence

Material requests and correspondence should be addressed to N.J.M. (nmaness@tulane.edu).

Figure legends

Fig. 1

Delayed serum viremia and altered leukocyte kinetics in CD8-depleted macaques. (**A**) Study design. Two animals of each cohort were depleted of CD8+ lymphocytes, and all animals were infected with a Brazilian isolate of ZIKV. Viremia was tracked over 30 days in cohort 1 and 14 days in cohort 2 before necropsy. Colors used in the timeline correspond to cohorts and treatment conditions. (**B**) Absolute CD8 T cell counts in blood, as determined by complete blood count (CBC). (*Top*): cohort 1; (*Bottom*): cohort 2 (consistent throughout). (**C**) NK cell frequency, as measured by flow cytometry. (**D**) Viral RNA in serum over infection. (**E**) Neutrophil-to-lymphocyte ratio (NLR), derived using total neutrophil and lymphocyte counts in blood from CBC data. (**F**) Fold change in NLR from 0 to 1 dpi among 4 rhesus and 4 cynomolgus macaques included in the present study, in addition to a previous cohort of 4 ZIKV-infected non-pregnant female rhesus macaques. The significant ($p \leq 0.05$) difference in NLR fold change was determined using a Mann-Whitney test.

Fig. 2

Differential monocyte-driven transcriptional profiles among CD8-depleted and nondepleted macaques. (**A**) Activation of downstream IFNα effector molecules in whole blood at 3 dpi relative to pre-infection. cyno. = cynomolgus (consistent throughout). **(B)** Fold regulation of antiviral gene expression in whole blood at 3 dpi, confirmed using a qRT-PCR array of 84 genes in the rhesus macaque genome. dep. = CD8-depleted; non. = nondepleted. **(C)** Principal component analysis (PCA) of antiviral gene expression in whole blood at 3 dpi. **(D)** Activation of downstream IFNα effector molecules in sorted CD14+ monocytes and CD14- PBMCs at 3 dpi. **(E)** qPCR confirmation of antiviral gene expression in CD14+

monocytes and CD14- PBMCs at 3 dpi. Gene induction is normalized to b-actin, and fold regulation is expressed relative to 0 dpi. **(F)** Antiviral gene expression in CD8+ and CD8- fractions of PBMCs from a nondepleted rhesus macaque at 3 dpi. Gene induction is normalized to b-actin, and fold regulation is expressed relative to 15 dpi. **(G)** Comparison of antiviral gene induction in cultured, ZIKV-infected MDMs (red) and the whole blood of nondepleted rhesus macaques at 3 dpi (black). Genes included in the qPCR array relate to toll-like receptor (TLR), nod-like receptor (NLR) or type-I interferon (IFN-I) signaling. resp. = responsive.

Fig. 3

Altered monocyte activation and frequency in CD8-depleted macaques. (**A-B**) viSNE analyses of monocyte activation in rhesus (A) and cynomolgus (B) macaques, as measured by CD169 mean fluorescence intensity (MFI). The viSNE clustering profile of monocyte subsets (*left*) correspond to cell populations in the CD169 MFI heatmaps in nondepleted and CD8-depleted animals over time (*right*). **(C)** summaries of CD169 expression in total monocytes. **(D)** Induction of genes related to myeloid cell activation at 3 dpi relative to pre-infection. (**E-G**) Frequencies of classical (E), nonclassical (F), and intermediate (G) monocyte subsets in rhesus and cynomolgus macaques over time.

Fig. 4

Compensatory adaptive immune responses in CD8-depleted macaques. (**A-B**) viSNE analyses of T cell activation in rhesus (A) and cynomolgus (B) macaques, as measured by CD69 expression. The viSNE clustering profiles of CD4 and CD8 T cell subsets (*left*) correspond to cell populations in the CD69 heatmaps in nondepleted and CD8-depleted animals at 1 & 10 dpi (*right*). (**C**) Proliferation of EM CD8 T cells in rhesus and cynomolgus macaques over time. (**D**) Proliferation of EM CD4 T cells in rhesus and cynomolgus macaques over time. **(E)** CD8 T cell responses in rhesus macaques, assessed by ICS of PBMCs stimulated with viral peptides derived from the indicated ZIKV proteins. CD8 T cell responses were identified by co-positivity for perforin and IFNγ. C = capsid; M = membrane; E = envelope; NS1 =

618 nonstructural protein 1 (consistent throughout). (**F**) Th1 responses, determined by ICS for IL-2 and IFNγ
619 co-positivity. (*Inset*): representative antigen-specific cytometry plots for R64357 at 30 dpi. (**G**) Serum
620 neutralizing antibody titers in rhesus macaques, represented as PRNT90. **(H)** Proliferation of B cells in
621 rhesus and cynomolgus macaques over time. **(I)** Activation of B cells in rhesus macaques over time.

622 ## Fig. 5

623 Enhanced tissue dissemination and neuropathology in CD8-depleted macaques. (**A-E**) Viral
624 dissemination in cynomolgus macaques, including lymphatic (A), neural (B) and reproductive (C) tissues,
625 as well as semen (D) and CSF (E). LN = lymph node; sub. wt. matter = subcortical white matter. **(F-H)**
626 Viral dissemination in rhesus macaques, including lymphatic, neural, and reproductive tissues (F), as well
627 as semen (G) and CSF (H). (**I**) R25671 brainstem (top) and lumbar spinal cord (bottom). *Top*: There is an
628 area of encephalomalacia (dotted region, left) adjacent to a vessel that exhibits medial thickening (arrow,
629 left). The area of malacia is characterized by dilated myelin sheaths with swollen axons (arrow, right) or
630 gitter cell infiltration (asterisks, right). H&E, Bar = 100 um. *Bottom*: The meninges surrounding the
631 lumbar spinal cord are multifocally infiltrated by aggregates of lymphocytes (arrows). H&E, Bar = 1 mm
632 (left) and 100 um (right). (**J**) R64357 sciatic nerve (top) and brainstem lesions (bottom). *Top*: Small
633 vessels within the sciatic nerve are surrounded by low numbers of lymphocytes (arrows). *Bottom*: A focal
634 glial nodule is present within the gray matter of the brainstem (dotted region, left) with dilation of
635 adjacent myelin sheaths and spheroid formation (arrowhead, right). H&E, Bar = 100 um.

636 ## Fig. S1

637 MT807R1 selectively depletes CD8+ lymphocytes with variable recovery. **(A)** Flow cytometric analysis
638 of CD8 T cell frequencies in PBMCs over time. **(B-C)** Absolute counts of CD4+/CD8+ double-positive T
639 cells (B) and (C) CD4 T cells prior to infection, determined by CBC.

Fig. S2

Comparison of virus and immune cell dynamics to a previous female cohort. Data from a previous cohort of ZIKV-infected non-pregnant female rhesus macaques is shown in gray, and data from rhesus macaques of the present study is overlaid. (**A**) Serum viral loads over the course of the studies. (**B**) CSF viral loads over the course of the studies. (**C-D**) Frequencies of neutrophils (C) and total lymphocytes (D) in whole blood over time, determined by CBC. **(E)** NLR, derived using total neutrophil and lymphocyte CBC data.

Fig. S3

Transcriptional responses correlate with serum viremia in nondepleted macaques. **(A)** Induction of genes related to leukocyte homing in whole blood at 3 dpi relative to pre-infection. **(B)** Activation of biological functions and disease-related pathways, as assessed by Ingenuity Pathway Analysis (IPA). **(C-D)** Patterns of antiviral gene induction at 1, 3, and 15 dpi in the whole blood of nondepleted (C) and CD8-depleted (D) rhesus macaques relative to pre-infection.

Fig. S4

CD8 depletion modulates monocyte phenotype during ZIKV infection. (**A-C**) Flow cytometric analysis of monocyte activation, as measured by CD169 expression in classical (A), intermediate (B), and nonclassical (C) subsets in rhesus and cynomolgus macaques. (**D**) Overall monocyte activation, as measured by CD69 expression. (**E-F**) Expression of CD95 in classical (E) and nonclassical (F) subsets.

Fig. S5

Reciprocal T cell responses are polyphenotypic. (**A-E**) Immunophenotyping of CD8 T cells in rhesus and cynomolgus macaques, including EM CD8 activation (A), CM CD8 activation (B) and proliferation (C), and naïve CD8 activation (D) and proliferation (E). **(F-J)** Immunophenotyping of CD4 T cells, including EM CD4 activation (F), CM CD4 activation (G) and proliferation (H), and naïve CD4 activation (I) and proliferation (J).

Fig. 1: Delayed serum viremia and altered leukocyte kinetics

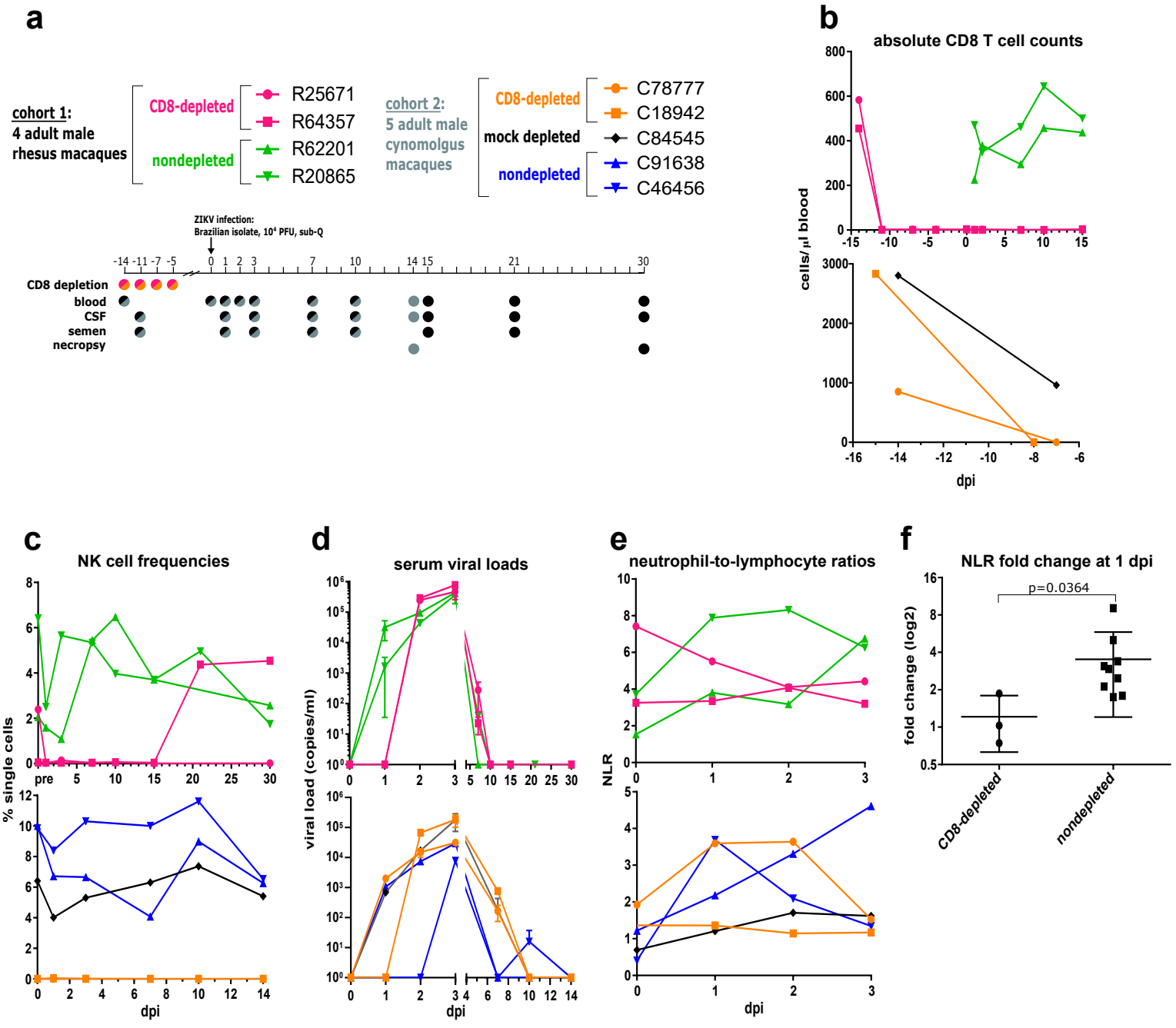

Fig. 2: Differential monocyte-driven transcriptional profiles

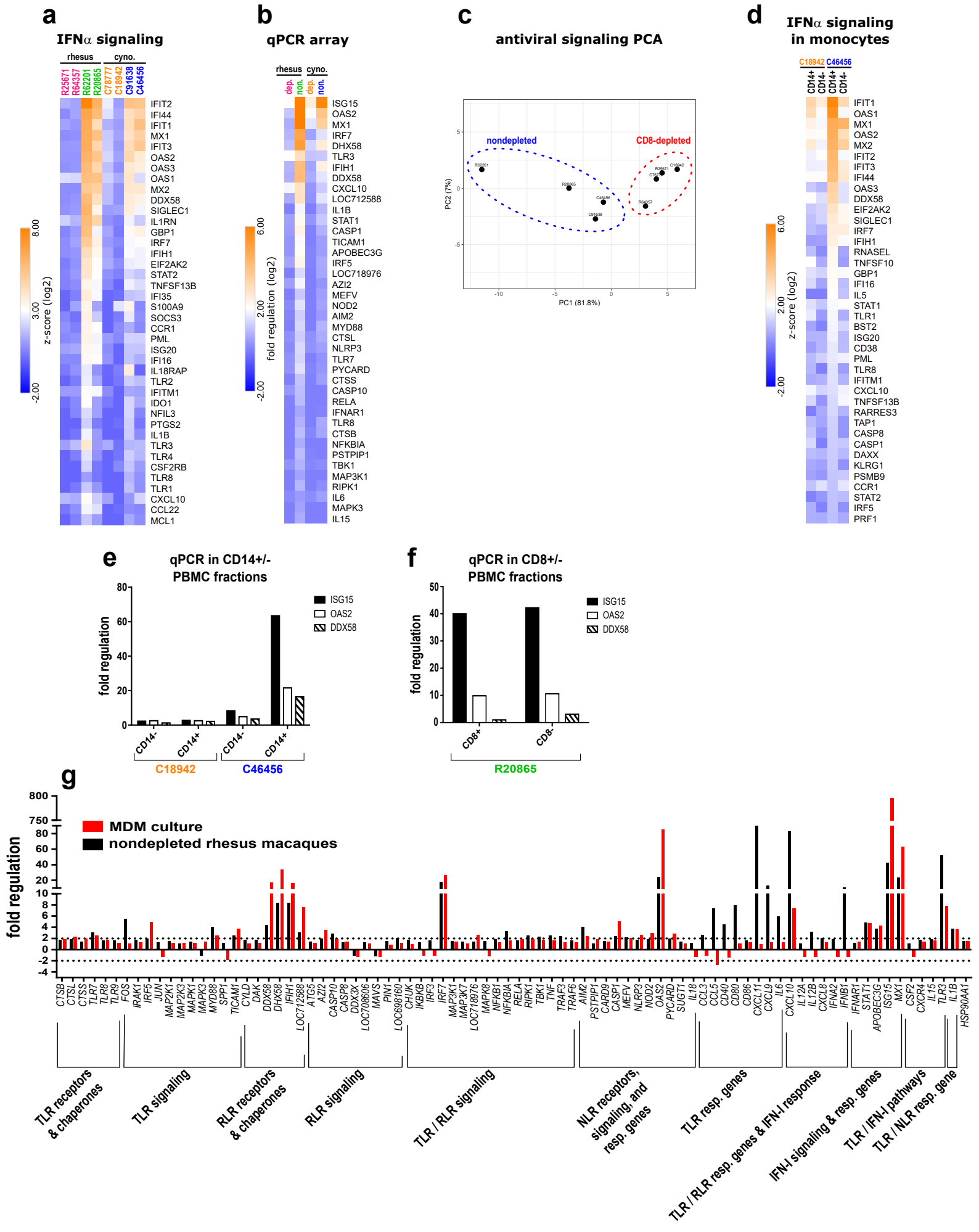

Fig. 3: Altered monocyte activation and frequency

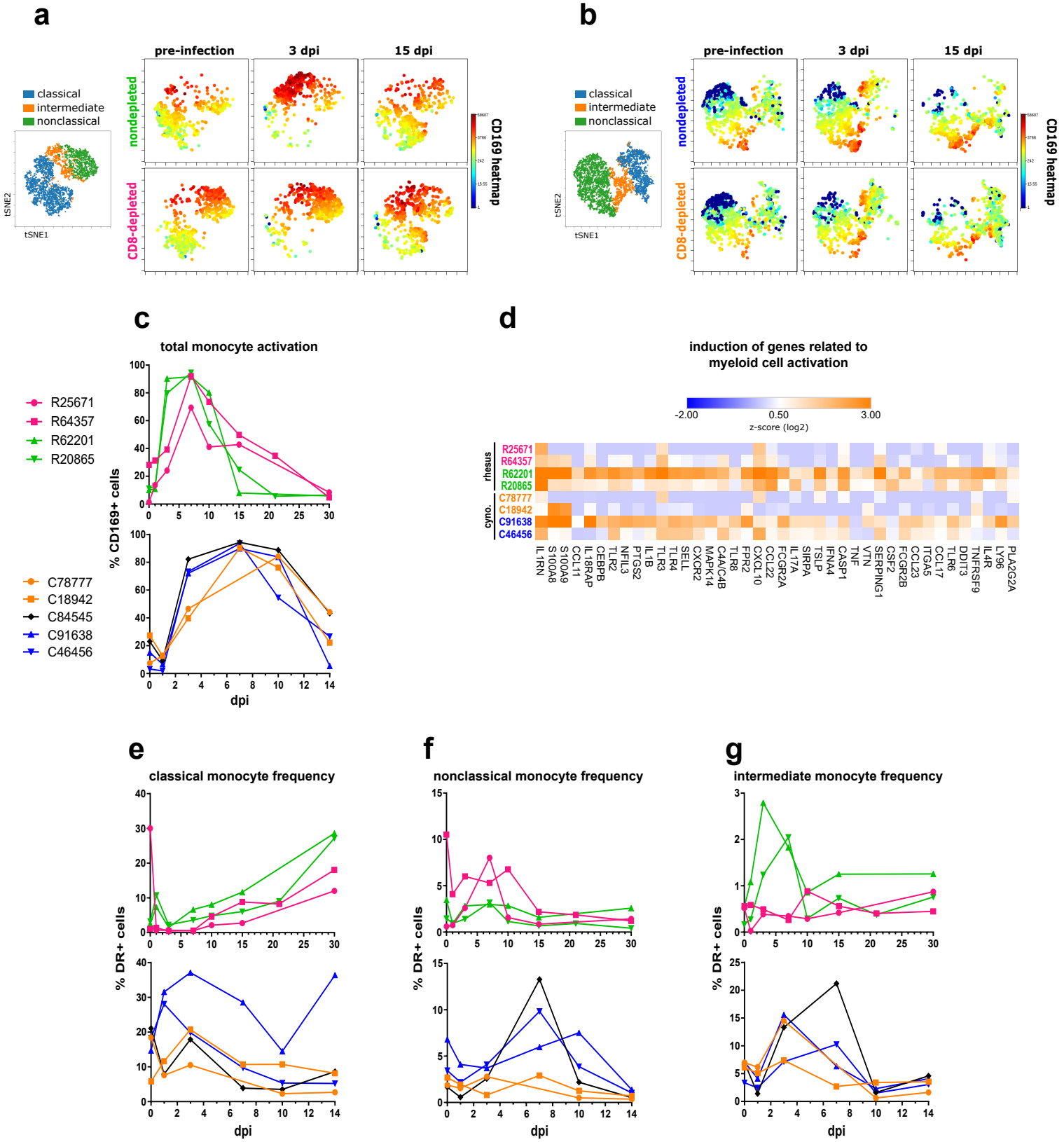

Fig. 4: Compensatory adaptive immune responses

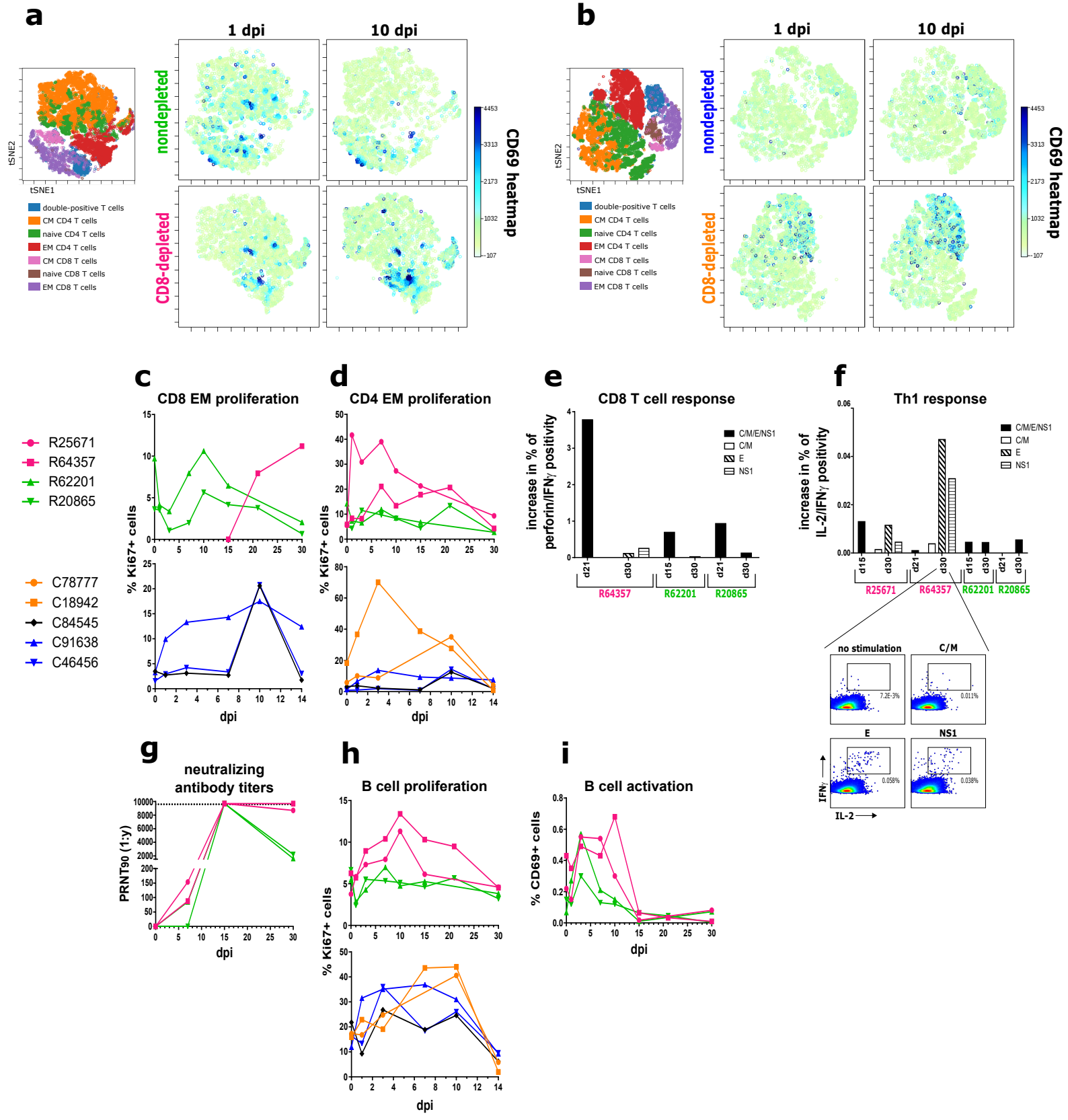

Fig. 5: Enhanced tissue dissemination and neuropathology